Measurement of the Force Produced by an Intact Bull Sperm Flagellum in Isometric Arrest and Estimation of the Dynein Stall Force

Kathleen A. Schmitz, Dana L. Holcomb-Wygle, Danial J. Oberski, and Charles B. Lindemann
Department of Biological Sciences, Oakland University, Rochester, Michigan 48309-4476 USA

ABSTRACT The force generated by a detergent-extracted reactivated bull sperm flagellum during an isometric stall was measured with a force-calibrated glass microprobe. The average isometric stall force from 48 individual measurements was $2.5 \pm 0.7 \times 10^{-5}$ dyne ($2.5 \pm 0.7 \times 10^{-10}$ N). The force measurements were obtained by positioning a calibrated microprobe in the beat path of sperm cells that were stuck by their heads to a glass microscope slide. The average position of the contact point of the flagellum with the probe was 15 μm from the head-tail junction. This average lever arm length multiplied by the measured force yields an estimate of the active bending moment (torque) of 3.9×10^{-8} dyne × cm (3.9×10^{-15} N × m). The force was sustained and was for the most part uniform, despite the fact that the flagellum beyond the point of contact with the probe usually continued beating. It appears that the dynein motors in the basal portion of the flagellum continue to pull in an isometric stall for as long as the motion of the flagellum is blocked. If dynein motors in the flagellum distal to the contact point with the probe were contributing force to the displacement of the probe, then the flagellar segment immediately past the point of contact would have to show a net curvature in the direction of the probe displacement. No such curvature bias was observed in the R-bend arrests, and only a small positive curvature bias was measured in the P-bend arrests. Our analysis of the data suggests that more than 90% of the sustained force component is generated by the part of the flagellum between the probe and the flagellar base. Based on this premise, the isometric stall force per dynein head is estimated to be 5.0×10^{-7} dyne (5 pN). This equals $\sim 1.0 \times 10^{-6}$ dyne (10 pN) per intact dynein arm. These values are close to the isometric stall force of isolated dynein. This suggests that all of the dynein heads between the base and the probe, on the active side of the axoneme, are contributing to the force exerted against the probe.

INTRODUCTION

The tail of a bull sperm cell is a single modified flagellum that derives its motility from an internal axoneme composed of a central pair of microtubules and nine outer doublets. The axoneme of a bull sperm is very similar in structure to the axonemes of all eukaryotic cilia and flagella. In eukaryotic flagella the force that is responsible for forming and propagating bends is produced by the molecular motor dynein. Dynein is arranged in a series of “arms” that project from eight of the nine outer doublet microtubules. The dynein arms generate motive force by attaching to and translocating the adjacent outer doublet microtubule.

Optical trapping studies have successfully measured the force produced by isolated dynein molecules interacting with immobilized microtubules (Ashkin et al., 1990; Wang et al., 1995). Other studies have estimated the force produced by dynein in disintegrating axonemes (Kamimura and Takahashi, 1981; Oiwa and Takahashi, 1988). To understand how cilia and flagella work it is necessary to understand the performance characteristics of the dynein motor protein within the confines of the flagellar axoneme as it carries out its intended function of generating motility. Computed models that attempt to duplicate the inner workings of cilia or flagella have mainly relied on estimates of the dynein force derived from hydrodynamic estimates of the active moments necessary to counterbalance the drag torque acting on the moving flagellum (for a review see Lindemann and Kanous, 1997). Until now, the only experimental study to directly measure the force produced by an intact cilium or flagellum used a compound cilium composed of ~20 axonemes (Yoneda, 1960). In that study, the cilium was positioned so that its motion was blocked by a force-calibrated microneedle. The displacement of the calibrated needle by the cilium allowed for the determination of the applied force. A value reported to be $(2.3–2.8) \times 10^{-4}$ dynes was measured at 20 μm along the cilium at 20°C.

In the current study we have adopted a similar approach to measure the force produced by a bull sperm flagellum. Triton X-100-extracted bull sperm models that are reactivated with Mg-ATP display normal motility (Lindemann and Gibbons, 1975). We made use of a recent observation that the reactivated sperm flagellum will arrest against an obstacle that prevents completion of the beat stroke (Holcomb-Wygle et al., 1999). We positioned reactivated sperm such that the beating flagellum arrested against a force-calibrated glass microprobe. The net viscous drag is reduced to zero during the arrest. Thus our measurement is a simple reflection of the force produced by the stalled flagellum. Bull sperm flagella are powered by a single internal axoneme. Therefore, the measurements of force and resulting torque can be taken as a true representation of the force produced by dynein within the context of a functional axoneme.

Received for publication 29 November 1999 and in final form 5 April 2000.

Address reprint requests to Dr. Charles B. Lindemann, Department of Biological Sciences, Dodge Hall of Engineering, Oakland University, Rochester, MI 48309-4476. Tel.: 248-370-3576; Fax: 248-370-4225; E-mail: lindeman@oakland.edu.

0006-3495/00/07/468/11 $2.00

MATERIALS AND METHODS

Microprobe production

To measure the force produced by a reactivated bull sperm flagellum, two different style microprobes (probes) were made using a Sutter Instrument Company (Novato, CA) P-87 pipette puller. Initially, the force probes were made with Warner Instrument (Hamden, CT) borosilicate glass capillary tubing (1 mm OD/0.58 mm ID) pulled to a taper length of 25–30 mm with a straight tip ~15 mm in length and a nearly uniform diameter (<1 μm). The long tapered end was broken off and attached to one end of another piece of capillary tubing with 5-min epoxy (Loctite Corp., Rocky Hill, CT). The tip was either inserted into the center of or placed alongside the capillary tubing such that the total length of the tip extending from the end was between 6 and 9 mm. To ensure that the tip of the probe was secure and unable to pivot, epoxy was applied so that it completely surrounded each tip, where it contacted the capillary tubing. Probes were discarded if the tips had epoxy on them anywhere other than where it was secured to the capillary tubing.

Further experiments used microprobes pulled from 1-mm borosilicate glass rod (Sutter Instrument Company). These probes had a final tip diameter approximately the same size as the capillary tubing force measurement probes (<1 μm), but the taper length was reduced to 9 mm. Shortening the taper length resulted in probes with an outside diameter greatest at the "shoulders" of the probe and tapering along the probe's length to a fine flexible tip ~3 mm long.

Patch-type/injection microprobes were made for the air-bubble microprobe calibration method. Borosilicate glass capillary tubing (1 mm OD/ 0.58 mm ID) was pulled to a taper length of ~7 mm. The distal 40–100-μm portion of the microprobe was broken off using a Narishige MF-79 microforge (East Meadow, NY), resulting in a 3–5-μm opening in the tip of the probe.

Microprobe calibration

Microprobes were mounted horizontally on the microforge that contained either a linear or a cross-hair ocular micrometer. In an effort to reduce interference from air currents during the calibration process, a Plexiglas cubicle was constructed to enclose the microforge. Low-frequency vibrations were minimized by placing the microforge on a three-inch marble slab separated from a tabletop by five size 8 silicone stoppers. Images of the calibration process were obtained with a GBC CCD-500B camera (CCTV Corp., South Hackensack, NJ) linked directly to a computer hard drive via a Matrox Electronic Systems (Dorval, Quebec, Canada) Meteor II card and Inspector 3.0 software.

Two different methods were used to calibrate the force measurement probes. The first method attaches polystyrene beads (Polysciences, Warrington, PA) of known density (1.05 g/ml) and diameter (45 and 90 μm) to the flexible tip of the probe by static electricity (Van Buren et al., 1994). The position of the microprobe's tip, with respect to the ocular micrometer, was noted at three separate times: before bead attachment (equilibrium position), with beads attached (displacement), and after bead removal (equilibrium position verification). There were some instances where the equilibrium position was disturbed during bead attachment. In those cases, the equilibrium position after bead removal was used for calculations, because removing a bead was less likely to disrupt the probe's position in the holder. Fig. 1 is a picture of one trial.

To accurately determine the force applied to the tip of the probe by the attached polystyrene bead(s), each bead was microscopically examined to determine the actual bead size. The actual force the bead(s) exerts on the probe is also dependent upon the position of the bead relative to the end of the microprobe. To determine the force applied at the tip of the probe, a small correction was made by dividing the total length of the microprobe by the functional length of the microprobe. The functional length of the probe is equal to the total length of the microprobe tip minus the lever arm. The lever arm is equal to the distance between the end of the probe and the bead's midpoint. For trials where more than one bead was attached, the mean lever arm for all beads was used to calculate the corrected force value.

The taper of the solid borosilicate probes, used later in the study, made the calibration much more sensitive to the exact position of the bead(s) on the shaft of the probe. The only probe of this type used in the measurement reported here was designated as probe D. The calibration of this probe included a regression analysis (Sigma Plot 4.0; SPSS, Chicago, IL) of the displacement of the probe tip as a function of the bead position offset from the tip. The resulting regression plot is shown in Fig. 2. Regression analysis of the probe not only had the distinct advantage of making the calibration specific for the position of contact with the probe, but also could be based on a very large number of individual calibration points. This helped to make the final calibration less subject to variations in bead size and air currents that might throw off an individual calibration point.

The other method of calibrating microprobes used air bubbles in lieu of polystyrene beads. To accomplish this, a watertight calibration chamber was constructed of two 75 mm × 38 mm microscope slides epoxied to a

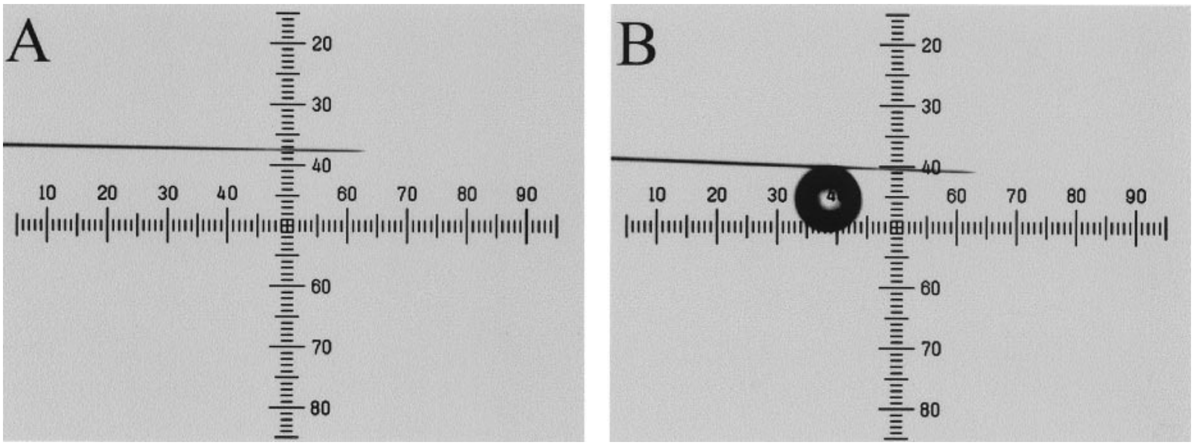

FIGURE 1 Polystyrene bead method of force-calibrating a solid glass rod microprobe. (*A*) Digital image of the glass microprobe at equilibrium. (*B*) After a 45-μm bead adheres to the probe by static electricity, it is displaced by the force of the bead. Each division on the cross-hair micrometer represents 4.1 μm. The offset of the bead from the probe tip was used to plot the regression of displacement as a function of bead position.

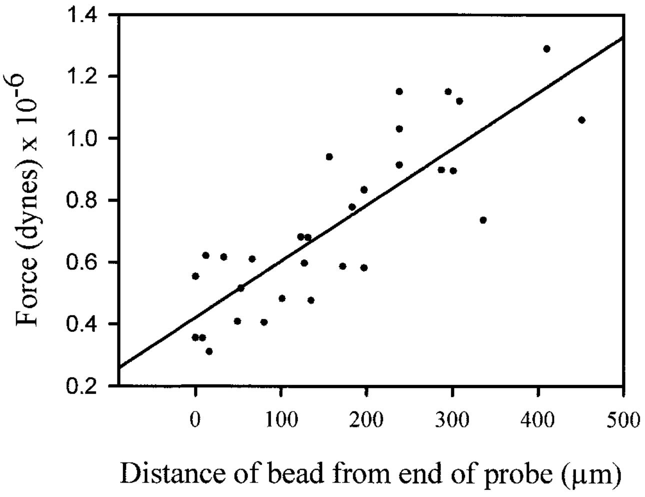

FIGURE 2 Regression analysis of bead force calibrations on a solid rod microprobe. The force exerted on a solid glass rod microprobe by 45-μm- and 90-μm-diameter polystyrene beads is plotted as a function of the distance the beads are from the tip of the probe. Linear regression analysis of the data reveals the relationship between the amount of force applied by the bead as the distance from the tip of the probe increases. $n = 30$.

13-mm-deep Plexiglas frame of equivalent dimensions (Fig. 3). To allow for probe insertion and manipulation, two 6-mm holes were located on opposing sides of the chamber's frame. A 1-cm hole on top, fitted with a silicone stopper, was used to fill and empty the chamber. The microprobe to be calibrated was positioned inside the chamber parallel to an air bubble microinjector probe such that its tip was located a few millimeters above the pore of the injector probe. To produce air bubbles, a Scherr-Tumico (St. James, MN) fine adjustment injector was loaded with a 27-gauge syringe. The syringe was filled with water and attached to a microinjector probe by lengths of Teflon tubing of increasing diameter (Cole Parmer, Vernon Hills, IL). As the bubbles ascended to the surface they collided with and adhered to the microprobe, displacing it upward from the equilibrium position. This displacement of the force measurement probe was measured, and the configuration of the probe was noted as well. The size of the air bubble was measured, and its placement on the probe was recorded. To find the necessary force to move the microprobe 1 μm, the force exerted by each air bubble was determined by calculating the volume of the bubble and the buoyancy that results from the displaced water volume.

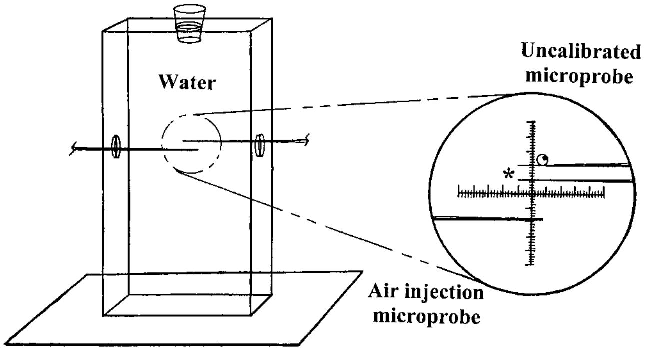

FIGURE 3 Underwater air-bubble calibration method. The design of the chamber for the air-bubble method of probe calibration is illustrated. A fill hole at the top of the chamber was sealed with a stopper. Two 6.5-mm holes on opposite sides of the chamber permitted the insertion of glass probes into the water without water loss and yet provided sufficient room to maneuver the probes. Air was injected through a probe with a 3–5-μm tip (*left*) to form a stream of small bubbles. The probe to be calibrated (*right*) was positioned in the bubble stream until a bubble was captured by surface tension. The diameter of the bubble was measured, as was the vertical displacement of the measurement probe, using a calibrated graticule in the microscope eyepiece.

The air bubbles produced by this method were three to five times larger than the 45-μm polystyrene beads. This larger force applied to the probe resulted in a greater probe displacement and necessitated correction for the angle of the probe with the horizontal by determining the vectorial component of the buoyancy force perpendicular to the probe axis.

Table 1 summarizes the calibration data for each of the four probes used to gather the data reported here. The number of force measurement data points collected with each probe is shown, and the calibration values and methods are summarized. Note the close agreement between the air bubble and bead calibration methods for probe C, as well as the agreement of pre- and postexperiment calibrations on this same probe.

Sperm preparation

NOBA, Inc. (Tiffin, OH), supplied bovine semen diluted to ~7.5 × 10^7 cells/ml in a milk-based extender. Samples were shipped weekly on ice in an insulated box and were received the next day in the laboratory, where they were stored at 0–5°C and used within 4 days.

Samples of bull sperm were washed from the milk-based extender by diluting 4 ml of the semen solution in 6 ml of sodium citrate buffer (0.097 M sodium citrate, 2 mM fructose, and 5 mM magnesium sulfate, pH 7.4). This mixture was then centrifuged at 960 × g for 10 min, and the supernatant was decanted. The remaining pellet was resuspended up to 10 ml with sodium citrate, centrifuged, decanted, and repeated once more. After the third wash, the pellet of cells was brought up to a final volume of 4 ml with sodium citrate. This was used as the stock sperm solution.

Reactivation

For each reactivation, 2–4 μl of stock sperm solution (dependent on concentration as it varied from week to week) was added to 3 ml of a reactivation mixture in a cell culture dish. The reactivation mixture (pH 7.8) contained 0.024 M potassium glutamate, 0.132 M sucrose, 0.02 M Tris-HCl (Fisher Scientific, Itasca, IL), 1 mM dithiothreitol (DTT) (Roche, Indianapolis, IN), 1 mM magnesium sulfate, 0.5 mM EGTA, 0.1% Triton X-100 (Pierce, Rockford, IL), 1 mM ATP (Fisher Scientific), and 0.003 mM cAMP (Roche). Reactivated sperm were gently pipetted into a glass slide chamber with an opening of 1 cm × 3 cm. This chamber was accessible to micromanipulation when placed on an Olympus IMT-2 inverted microscope.

Force measurements

To minimize extraneous probe oscillation due to low-frequency vibration, all experiments were performed on a MICRO-g vibration isolation table (Technical Manufacturing Corp, Peabody, MA). Experiments were viewed with phase-contrast illumination and videotaped with a Mitsubishi S-VHS video recorder and a GBC 505-E CCD camera (CCTV Corp.) mounted on the microscope. Data were obtained by making tracings of the videotaped recordings played back on a Panasonic monitor (model WV-5410). These tracings were made by using the jog shuttle feature of the VCR with a framing rate of 30 frames/s. We used Snappy 3.0 video snapshot framegrabber (Play Inc., Rancho Cordova, CA) and Corel Photo-Paint 8 (Ottawa, ON, Canada) to produce photos of individual frames (Fig. 4).

TABLE 1 Calibration data for glass microprobes

Probe	Type of borosilicate glass	No. of calibrations	Pre/post usage*	Calibration method	Mean force of calibrations (dynes/μm)	No. of force measurements
A	Capillary tubing	3	Pre	Polystyrene bead	1.24×10^{-5}	4
B	Capillary tubing	15	Pre	Air bubble	8.24×10^{-6}	12
C[†]	Capillary tubing	10	Pre	Air bubble	8.13×10^{-6}	
	Capillary tubing	10	Post	Air bubble	8.24×10^{-6}	8
	Capillary tubing	10	Post	Polystyrene bead	7.36×10^{-6}	
D[‡]	Solid rod	30	Post	Polystyrene bead	4.30×10^{-6}	24

*Pre/post usage defines when calibrations were done in relation to the experimental stall force measurements.

[†] A mean value of all three calibration methods (7.91×10^{-6} dynes) was used for calculating stall forces.

[‡] Linear regression analysis used to determine individual calibration force values.

We selected for manipulation sperm that had adhered to the glass slide by their head, showed unobstructed movement of the flagellum, and exhibited a normal beat pattern. The tip of the microprobe was then positioned in the path of the beating flagellum so that the midline of the flagellum's long axis was nearly parallel to the tip of the probe. Movement of the microprobe was controlled by a de Fonbrune-type joystick-operated micromanipulator (Technical Products International, St. Louis, MO). The microprobe was then moved slowly from either the midline of the beat or down the length of the flagellum, or both, until the point at which an isometric stall of the beat was obtained in either the principal (P) or reverse (R) direction. The P-bend direction was defined by the side of the beat where the flagellum makes the greatest excursion and where it develops the greatest extreme of curvature. P and R stalls were named for the direction of flagellar movement at impact with the probe.

In all cases, the angle of the sperm cell's midline, relative to the probe, was measured with a protractor. Instances in which the sperm flagellum was 40° or more from parallel with the probe were not used as data. For angles between 1° and 39° a correction of the measured force value was

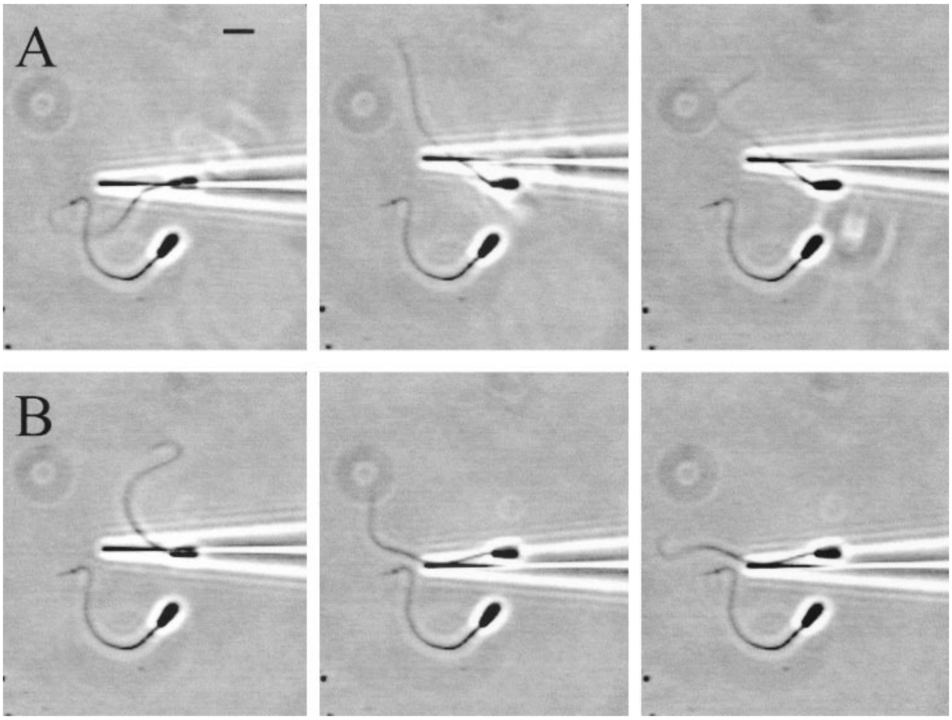

FIGURE 4 Sustained force and probe displacement produced by a bull sperm flagellum during an isometric stall. A Triton X-100-extracted bull sperm was reactivated with 1 mM ATP and subjected to manipulation by a force-calibrated glass microprobe to obtain an isometric stall of the flagellar beat. The same cell is shown in all six photos. (*A*) The process of an isometric arrest of the flagellum in the principal (P) bend direction of the beat. (*B*) A stall in the reverse (R) bend direction. *Left*: A bull sperm stuck to a glass slide by its head with the flagellum freely beating in both the P-bend (*top photo*) and R-bend (*bottom photo*) directions. The force-calibrated microprobe is at the equilibrium position. *Center*: An isometric stall of the flagellum and concomitant displacement of the probe in both directions, P (*top*) and R (*bottom*), of the beat. *Right*: Sustained force production by the flagellum during the isometric stall is evident from the maintained displacement of the probe. The same stalls shown in the center photos are shown 39 frames later in the P-bend direction (*top photo*) and 16 frames later in the R-bend direction (*bottom photo*). 1 frame = 0.033 s. Note the portion of the flagellum distal to the point of contact with the probe continues to beat, while the proximal portion maintains the original configuration. The stall shown in *A* was traced to make Fig. 5. Bar = 10 μm.

made. The correction factor is equal to the measured force value (dynes/μm)/cosine of the measured angle. Fig. 5 is a tracing of a cell not in contact with the probe (equilibrium position) with an overlay of the same cell arrested against a calibrated probe (isometric stall). The measured displacement, intersection angle of the probe and flagellum, and lever arm are shown. The displacement of the probe on the video monitor ranged from 11 to 47 pixels and averaged 24 pixels. This corresponds to a distance of ~4.0 μm on the microscope slide.

Curvature measurements

Measuring the radius of curvature of the flagellum was obtained by two different methods corresponding to the part of the flagellum that was either proximal or distal to the point of contact with the probe. The proximal curvature had to be estimated because the curvature was never uniform over the basal segment in an arrest. To estimate the proximal curvature, the change in angle of the flagellum from the base of the head to the contact point with the probe was divided by the length of the flagellum from the head to the probe. Curvature of the distal flagellum was measured directly by matching computer-generated concentric circles of known radius (cm) to the curve of the first 10 μm of flagellum past the probe and correcting for screen magnification (Holcomb-Wygle et al., 1999). Measurements were limited to cells that were in focus. Each cell was measured at the two extremes of the flagellar beat.

RESULTS

Triton X-100-extracted bull sperm models reactivated with 1 mM Mg-ATP were positioned so as to arrest pushing against a calibrated glass microprobe. The heads of reactivated sperm stick readily to a glass slide while their flagellum continues to beat. We selected sperm that had the long axis of their heads oriented roughly parallel to a force-calibrated microprobe mounted on a micromanipulator. The microprobe was positioned so that it impeded the beat of the flagellum. In this configuration, the application of force by the flagellum to the microprobe is roughly perpendicular to the shaft of the microprobe. When the probe obstructed the flagellum in the middle of the range of motion of the beat, an arrest resulted, with the flagellum pushing against the probe with a maintained force. This behavior is shown in Fig. 4. Note that the part of the flagellum beyond the contact point with the probe often continues to beat. However, the maintained displacement of the probe attests to a sustained lateral force exerted against the probe. Fig. 4 also shows that arrest and sustained force production were observed when the motion was interrupted in both the P and R beat directions.

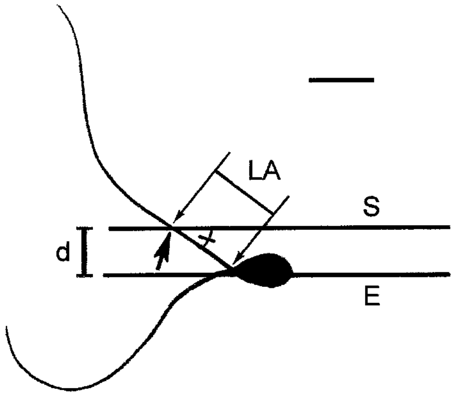

FIGURE 5 Measurement of force produced by an intact bull sperm flagellum in an isometric stall. A tracing of a bull sperm flagellum freely beating was overlaid by a tracing of the same flagellum in an isometric stall of the beat in the principal (P) bend direction. E, The position of the microprobe at equilibrium. S, The location of the same probe during the isometric stall. The large arrow indicates the point of contact with the probe and the direction of the beat before contact with the probe. The lever arm length (LA) measured is the distance between the two small arrows. The angle of the sperm cell's midline relative to the probe is indicated. The tracing was produced from the same stall as shown in Fig. 4 *A*. Bar = 10 μm.

Occasionally the arrested flagellum was not parallel to the shaft of the microprobe. For the purpose of force estimation such deviations from a parallel configuration were corrected by finding the angle of intersection of the flagellum with the microprobe shaft (as illustrated in Fig. 5) and dividing the measured displacing force by the cosine of this angle. Measurements in which the intersection angle exceeded 40° were excluded from the data. A summary tabulation of the force measurements is provided in Table 2.

The mean arrest force of the flagellum against the probes for all cases (both P and R bend arrests) was $(2.5 \pm 0.7) \times 10^{-5}$ dyne ($n = 48$). The best-situated arrest geometry was obtained in the R bend arrests, as shown in Fig. 5 *B*. Pooled data from only R bend arrests yields a mean value of $(2.46 \pm 0.59) \times 10^{-5}$ dyne ($n = 33$). The result from P bend arrests was similar but somewhat larger at $(2.66 \pm 0.86) \times 10^{-5}$ dyne ($n = 15$). The difference in the P and R force values is not significant. The difficulty in getting favorable measurement geometry in the P bend arrests adds some uncertainty to the true mean, as seen by the larger standard deviation of the mean. This results from the fact that the natural curvature of the flagellum during the P bend phase of the beat cycle tends to wrap the flagellum around the probe. This in turn causes it to slide up or under the shaft of the probe, thereby increasing the angle of intersection at the point of arrest (as seen in Fig. 4).

The measurements of force applied by the flagellum to the microprobe also allow us to determine a value for the bending torque generated by the beating flagellum. The point of application of the force to the glass probe was on average 15 μm from the flagellar base (Table 2). This mean value for the flagellar lever arm multiplied by the mean force applied to the probe yields an average bending torque (active moment) of $(3.9 \pm 1.6) \times 10^{-8}$ dyne × cm at the flagellar base. Measurements where the flagellar lever arm was longest (22–26 μm) yielded a greater bending torque than measurements at the shortest lever arm lengths (10–12 μm). The relationship of torque to lever arm is displayed graphically in Fig. 6. The result suggests that there is a general trend toward greater torque as the lever arm is increased.

TABLE 2 Measurement of force of a bull sperm flagellum during an isometric stall

	P arrests	R arrests	Totals for P and R
n (isometric stalls)	15	33	48
No. of frames of stall ± SD	48 ± 103	18 ± 17	40 ± 66
Force (dynes) ± SD	$2.66 \times 10^{-5} \pm 0.86$	$2.46 \times 10^{-5} \pm 0.59$	$2.52 \times 10^{-5} \pm 0.68$
Lever arm (μm) ± SD	16 ± 3.6	15 ± 3.6	15.3 ± 3.8
Torque (dyne × cm) ± SD	$4.26 \times 10^{-8} \pm 1.9$	$3.67 \times 10^{-8} \pm 1.3$	$3.89 \times 10^{-8} \pm 1.6$

Over the course of this study two fundamentally different ways of fabricating the measurement probes were employed. In the first method, very long (25–30 mm) relatively uniform threads of tubular glass were produced, then broken off and mounted with epoxy to the end of a large rigid glass capillary tube. In these probes, virtually all of the flexing of the glass was far from the site of measurement. In the second and later method, a solid glass rod was used to fashion the probes, and the tip was pulled to a workably short (9 mm) and rapidly tapering fine microprobe. These finer, shorter probes were more flexible at the tip, and therefore the point of application of the force in relation to the tip was a factor in determining the correct force calibration value. When the force versus displacement regression was found by multiple position calibration, an applicable calibration value could be found for any point of force application along this probe (see Fig. 2).

Underwater calibration using the buoyancy of small air bubbles gave a calibration similar to that found with polystyrene beads when carried out on the same probe, as shown in Table 1. This assures us that the hydration of the glass does not substantially alter the effective stiffness of the probes under actual measurement conditions.

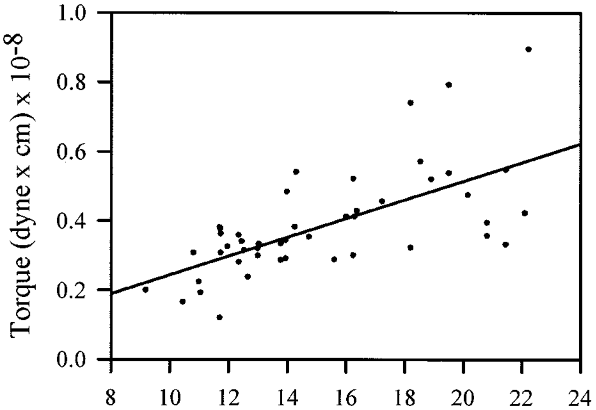

FIGURE 6 Regression analysis of torque versus lever arm for principal (P) and reverse (R) bend isometric stall force measurements. The amount of torque produced by a bull sperm flagellum during an isometric arrest of the beat is plotted as a function of the length of the lever arm. The lever arm is equal to the length of flagellum between the head-tail junction of the sperm cell and the point of contact with the force-calibrated microprobe as shown in Fig. 5. Linear regression analysis of the data shows that as the lever arm length increases, the amount of torque produced also increases. $n = 48$.

The force data collected by the first method of probe fabrication gave an average of $2.6 \pm 0.6 \times 10^{-5}$ dyne ($n = 24$). The average force found with the second method of probe fabrication (solid rod) was $2.4 \pm 0.7 \times 10^{-5}$ dyne ($n = 24$). The data collected with the two different methods of probe fabrication show that our results are independent of a specific probe geometry or calibration method.

The flagellum beyond the point of contact with the probe was often quite active. To understand the contribution of this distal activity to the force and torque measurements, we examined the relationship of this activity with the force on the probe. For this analysis we examined the situation in 23 stalls of longest duration (>30 frames) selected from the 48 force measurements. The selection of the longest stalls was necessary to permit accurate scoring of the beating behavior of the distal flagellum and accurate estimation of the variation in lateral displacement of the probe. The results are given in Table 3. There is seldom a strong net curvature of the first 10 μm of flagellum beyond the blockage point. Four of the 23 cases showed a persistent curvature in the portion of the flagellum immediately distal to the probe, and of these, two were in the direction of the block and two were in the opposite direction. All four that did curve strongly showed curvature in the P-bend direction despite the fact that two were P-blocks and two were R-blocks. In all but those four cases the net curvature oscillated between

TABLE 3 Behavior of the distal flagellum during isometric stalls

	P arrests	R arrests	Totals for P and R
n (isometric stalls)*	8	15	23
Net flagellar curvature[†]			
Positive	2	0	2
Negative	0	2	2
Neutral	6	13	19
Oscillating waveform[‡]	4	13	17
Erratic waveform	4	2	6
Detectable wobble	2	4	6[¶]
No wobble[§]	6	11	17

*Stalls that lasted for 30 frames or longer.

[†] The first 10 μm distal to the block point. Positive is in the direction of the sustained force.

[‡] Showed repetitive movement during the block.

[§] Below the level of discrimination for measurement.

[¶] Mean wobble as a percentage of the average sustained force = 15%.

slightly positive and slightly negative in time with the movement of the distal part of the flagellum. In the six cases that showed the strongest oscillation in probe position we measured the wobble in the probe position produced by the distal oscillation. In these six cases the probe displacement in response to the distal movement of the flagellum averaged 15% of the mean sustained displacement. This gives us an estimate of the upper limit that distal beating activity influences the displacement of the probe. The absence of a strong curvature bias in all but four of the 23 cases examined indicates that this variable contribution is alternately additive and subtractive from the mean value. To further confirm that this is a valid conclusion, we also measured the curvature maxima of the 10 μm of flagellum just beyond the probe contact. The data shown in Table 4 show that there is no curvature bias in the R-arrests and only a small bias in the direction of the block in the P-arrests. The maximum estimate obtained from the wobble data translates into a maximum variation of ±8% superimposed on the mean sustained force. This interpretation, which is based on reasonable assumptions, suggests that the mean sustained force reported here originated almost entirely from dyneins located between the base and the point of contact with the probe.

ANALYSIS AND MODEL

Interpretation of the force data requires a suitable model of the transmission of forces within the mammalian sperm axoneme. The sliding doublet model of axonemal function is well substantiated from experimental data and has been put into a computational model by Brokaw (1972). In this view of axonemal functioning the nine outer doublets constitute inextensible, but flexible, rods. Force generated between the doublet pairs by the action of the dynein arms is transmitted to the basal body, which serves as an anchoring structure. Therefore, the force felt at the base is a summation of the force contributed by the dyneins pulling (or pushing) on the doublet along its length. The flagellum bends in a direction perpendicular to the central pair of doublets, which define the axis of the beat. The dynein arms between doublets 1–5 contribute force to bend the axoneme in one bending direction, and the dyneins on doublets 6–9 contribute force for bending in the opposite direction. Force is generated between doublets by the action of the dynein arms between the pair. However, the piggyback arrangement of the doublet pairs leads to the serial transmission of force to the first and last elements in the active group of doublets (see Fig. 7). This results in the force that develops between each pair of doublets ultimately being transmitted to the doublets on the innermost and outermost extremes of a developing bend, namely doublet 1 and doublets 5–6 on the opposite side. Therefore, in the simple eukaryotic axoneme, the force couple has a working diameter consistent with the spacing between doublets 1 and 5–6. The bending torque that is responsible for propelling the active movements of the flagellum is thus calculated by the magnitude of this lever arm times the linear tension (and compression) on doublets 1 and 5–6. This view does presume equal participation of the intervening doublet pairs; if one or more pairs of doublets were not contributing to the bending torque, it would reduce the effective working diameter. This would have the result that greater linear force (and force per dynein arm) would be necessary to produce the observed external torque.

For the purpose of our analysis we have adopted the standard sliding doublet view of the axoneme with only minor modifications that are known features of the bull sperm axoneme. A description of this model as applied to bull sperm has been published (Lindemann, 1996). In the bull-sperm-specific model, the nine outer doublets are attached to the outer dense fibers (ODFs) along most of their length, as shown schematically in Fig. 7. This structural relationship was demonstrated in transmission electron microscopy studies of mammalian sperm and is generally accepted (Lindemann and Gibbons, 1975: Olson and Linck,

TABLE 4 Geometry of a bull sperm during isometric stalls of the flagellum

	Arrest direction*	n	Mean ± SD (radians/cm)
Proximal flagellum			
Head to flagellar insertion angle (radians)	P	15	$0.44 \pm 0.14^{\dagger}$
	R	33	0.10 ± 0.07
Base to probe curvature (radians/cm)	P	15	$304 \pm 185^{\ddagger}$
	R	33	-4 ± 151
Distal flagellum			
Curvature of 10-μm segment adjacent to probe (radians/cm)	P maximum	10	533 ± 237
	P minimum	10	-268 ± 176
	R maximum	24	488 ± 434
	R minimum	24	-415 ± 447

*P, principal; R, reverse.

[†] Significantly different from R head to flagellar insertion angle (*t*-test), $p < 0.01$.

[‡] Significantly different from R mean proximal curvature (*t*-test), $p < 0.01$.

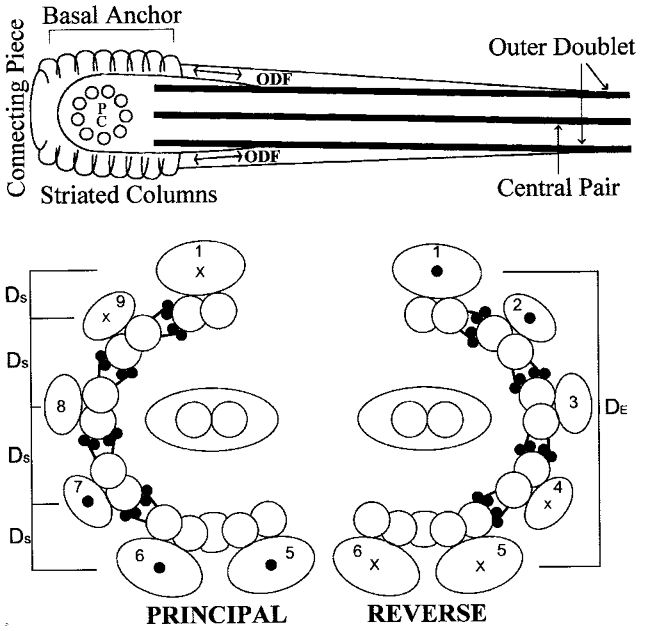

FIGURE 7 A functional schematic diagram of the mammalian sperm axoneme. (*A*) In the mammalian sperm axoneme, the outer microtubule doublets are not anchored into a basal body at the flagellar base, but are attached to the outer dense fibers (ODFs) along much of their length. However, the ODFs are affixed to the striated columns of the connecting piece. Consequently, when the doublets slide by the action of the dynein motors, the resultant force is transmitted through the ODFs to the connecting piece (*arrows*). The connecting piece assumes the role of a basal anchor replacing the basal body, which disassembles during spermatogenesis. (*B*) The sliding induced by the dynein-tubulin cross-bridge cycle during formation of principal and reverse bends results in maximal sliding displacement between elements 1 and 5–6. Unlike in simple flagella, the magnitude of interdoublet sliding is not determined by interdoublet spacing, but is dictated by the inter-ODF distances in the bending plane (identified as D_S in the diagram). Force will also be transmitted to the ODFs, causing the greatest torque to develop from the force imparted to elements 1 and 5–6 because they exhibit the greatest separation (the effective diameter, D_E). ● and ×, Thrust in the directions into (●) and out of (×) the page, as if the axoneme were being viewed baseward. This is an adaptation of a figure previously published in Lindemann (1996). Reproduced with permission.

1977). Furthermore, in axonemes that are disintegrated by microtubule sliding after limited proteolysis, the outer dense fibers and doublets remain attached at the basal end of the disrupted flagellum. This attachment is mediated by the structure called the connecting piece. It is a curious fact first observed by Fawcett and Phillips (1969) that the basal body of mammalian sperm flagella vanishes before the sperm mature. Therefore, forces from the doublet microtubules must be transmitted to the basal anchor (which is the connecting piece) via the microtubule attachments to the outer dense fibers, as shown schematically in Fig. 7. In our force measurement experiments, the full torque exerted against the microprobe must be generated by the forces transmitted to the connecting piece that is anchored in the sperm head, the sperm head being securely adhered to the glass slide. Thus, in this model, force to support the measured torque must come from the tension and compression on the most widely spaced ODF elements near the flagellar base. The working diameter separating these elements has been measured from transmission electron microscopy cross sections and is $\sim 3.25 \times 10^{-5}$ cm (center to center) near the flagellar base (Lindemann, 1996). It should be noted that if one does not assume that this is the proper working diameter, then the linear force on the doublets must be considerably larger, so we are adopting the most conservative and best-substantiated position.

This model of the internal force distribution has been used to relate the measured force and torque to the internal force generated across doublets 1 and 5–6. Because the arrangement of the doublets is serial, as shown in Fig. 7, each doublet pair between 1 and 5–6 must bare the same transmitted tension. If this assumption is not correct, then the tension on a smaller number of participating doublet pairs would be considerably greater. Once again, we have adopted the most conservative interpretation.

An additional factor that must also be considered is the elastic rigidity of the flagellar structure and how much of the internal bending torque is being spent against the elastic stiffness of the flagellar structure. Although the flagellum in most of the R-bend arrests is relatively straight between the base and the probe, there is often noticeable curvature of the flagellum in the P-bend arrests (Table 4). We have measured the overall change in angle of the flagellum from the base to the probe impact point, and it is often significant in the P-bend arrests. The change in angle divided by the length of the flagellar segment between the base and the probe was used to estimate the average curvature of the basal segment of arrested flagellum as given in Table 4. Multiplying this average curvature by the basal flagellar stiffness ($\sim 4.0 \times 10^{-12}$ dyne $\times$ cm^2) as estimated by a dynamic analysis (Lindemann et al., 1973) yields an elastic moment opposing the active torque of 1.2×10^{-9} dyne $\times$ cm in the P-bend arrests. Because both the probe and this elastic moment are opposing the movement of the flagellum, this moment of elasticity must be added to the torque exerted by the probe against the sperm to find the total internal active torque. Consequently, this adjustment would make the internal torque slightly larger (4%) than the directly measured value in the P-bend direction but smaller than the limit of error of the measurements. It is a negligible factor in the R-bend direction ($<1\%$), because the flagellum has little curvature in this arrest configuration (Table 4).

The model we are using also does not account for the possibility that there is some tilting of the connecting piece relative to the flagellar axis, especially when it is under dynamic tension. In fact we do see a relatively sharp angular displacement of the flagellum to the axis of the head in the P-bend arrests (head tilt), but we do not see any significant head tilt in the R-arrests (Table 4). The geometry of the head flagellar junction at the connecting piece is such that tilting the connecting piece would reduce the diameter between the outer dense fibers and consequently reduce the working diameter for the internal torque generation. While such a phenomenon remains a possibility, it is again noteworthy that it could increase, not decrease, an estimate of the internal force on the doublets.

The information on the flagellar geometry summarized in Table 4 and presented above shows that the R-bend arrests are the closest to an ideal condition for an accurate measurement of the internal force on the doublets and hence of the dynein force. The R-bend measurements show the least deviation from the case of a simple lever arm. The R-bend arrests have the best geometry for unambiguous interpretation, and the data from these arrests have the smaller scatter, as judged by the standard deviation.

If we can determine, with some certainty, what portion of the flagellum actively contributes force to the probe under our measurement conditions, then it would be possible to estimate the force per dynein arm in an intact flagellum. The dynein arms that lie between the flagellar base and the point of contact with the probe should theoretically generate most, if not all, of the bending torque that pushes against the measurement probe. The reason for this is that beyond the contact point most, if not all, of the bending torque should be free to reach a Newtonian equilibrium with the dynamic stiffness of the flagellar shaft and the viscous drag. This assumption from first principles of physics has been applied in all earlier analyses of flagellar motion (for a review see Lindemann and Kanous, 1997). The relationship we found for torque verses lever arm (Fig. 6) supports this idea. The measured torque tends to increase linearly with increasing distance of the measurement point from the base of the flagellum. However, there is still one condition that could render the assumption invalid. If the curvature of the flagellum immediately beyond the impact point with the probe shows a consistent curvature bias, then it must be inferred that the doublets are under tension at the probe contact point. The reasoning is as follows. If the region of the flagellum just distal to the probe shows a strong maintained curvature, the doublets in the curved region must be under linear tension as a necessary condition for maintaining the curve. The tension must be transmitted to the doublets just basal to the probe, because the doublets in the curved region are continuous with the doublets immediately basal to the probe contact point and would add to (or subtract from) the torque pushing on the probe. Therefore, the contribution to the sustained force coming from dynein motors distal to the blockage point can be directly assessed by examining the net curvature of the flagellum immediately beyond the block point. We have examined the situation in the 23 longest lasting stalls selected from the 48 force measurements (Table 3). We collected data on the curvature of the flagellum and the maximum variation in probe displacement that is correlated with the distal motion of the flagellum. There is very little sustained curvature, and the variation in probe displacement is small and oscillates about a larger sustained displacement. Both results suggest that the sustained force pushing on the probe comes only from the dyneins between the probe and the flagellar base. This is most certainly true in the R-arrests, where net curvature beyond the probe contact was either near zero ($n = 13$) or opposite the direction of the block ($n = 2$) and would therefore subtract from rather than add to the total sustained force (Table 3). The same conclusion can be drawn from the measurements of the maximum and minimum curvatures measured for 10 P-arrests and 24 R-arrests where we could see the flagellum well enough to take curvature measurements in the region just distal to the probe. These data are shown in Table 4. As can be seen, there is almost no net curvature bias in the R-arrests (<100 radians/cm). There is a small (~270 radians/cm) forward bias in the P-arrests. Multiplying this by the flagellar stiffness yields an elastic torque of only 1.1×10^{-9} dyne × cm. This represents a torque contribution of only 3% of the total measured value. Therefore, by this means of estimation, the distal dynein bridges are contributing at most 3% of the torque exerted against the probe and only in the P-bend arrests.

Based on only the R-arrest force data and the average lever arm, we find an active moment of $3.7 \pm 1.3 \times 10^{-8}$ dyne × cm. This average bending torque value divided by the basal working diameter of 3.25×10^{-5} cm (from Lindemann, 1996) gives a tension on doublets 1 and 5–6 of 1.1×10^{-3} dyne. The distribution of dynein arms along the flagellum is known to be ~70/μm on each doublet. This yields a stall force of 1.0×10^{-6} dyne per arm (10 pN), assuming all arms participate in a stall. If one assumes that fewer arms participate at any instant, then the force per arm would be larger still. Most reports of the dynein force have been given in force per dynein head. If total units of dynein heavy chain are used instead (~150 dynein heads/μm on each doublet), then the force in our determination would be 4.9×10^{-7} dynes/dynein head (~5 pN).

DISCUSSION

This study provides the first direct measurement of the force and the bending torque produced by a single intact flagellum in the act of beating. The method of measurement takes advantage of the flagellar tendency to arrest while pushing against a restrictive obstacle (Holcomb-Wygle et al., 1999). Therefore, the measured force and torque are essentially the equivalent of an isometric stall force as has been defined in whole muscle. It is known from other studies on isolated molecular motors and intact muscle that the isometric stall force is generally the maximum value of force that can be produced by the motor protein. This should be kept in mind when comparing the values reported here to the dynamic estimates obtained from moving flagella. The theoretical framework provided by Brokaw (1999) suggests a plausible relationship between the force and velocity that is a good match with experimental observation. That analysis suggests that the stall force must be significantly larger than the dynamic value, especially for the inner dynein arms.

The value of 10 pN per dynein arm is not very different from the laser trap measurements of the stall force of single dynein arms (~6 pN) reported by Shingyoji et al. (1998). The estimates are actually remarkably close, considering the vastly different experimental conditions and the use of two totally independent measurement techniques.

The only other measurement that has been made on an intact beating eukaryotic flagellum or cilium was that of Yoneda (1960) on the compound abfrontal cilium of *Mytilus edulis.* At distances greater than 20 μm from the base, the average torque generated by the cilia was 3.9×10^{-7} dyne $\times$ cm. The working diameter of each ciliary axoneme is $\sim 2 \times 10^{-5}$ cm. Assuming that there are 20 functional axonemes (as estimated by Yoneda, 1960), we can divide the measured torque by 20 and apply the same method to estimate the dynein force as used above for the bull sperm data. The data reported by Yoneda also showed that the torque did not increase beyond 20 μm. Therefore, 20 μm can be taken as the maximum contributing length of dynein bridges. With this assumption, the calculation yields an estimate of the force per dynein arm of 6.5×10^{-7} dyne (~7 pN) and a force of 3×10^{-7} dyne (3 pN) per dynein head for the compound cilium. However, it should be kept in mind that the comparison is very tentative. It was also reported that one individual cilium generated a torque of 8×10^{-7} dyne $\times$ cm, which would yield a force per arm slightly higher than our estimate! The compound cilium is composed of many axonemes. Not only is the number of axonemes in a specific cilium indeterminate, but there is no way to know if all are functional, leaving uncertainty about the correct number of axonemes for the estimate. Thus the average value determined from the earlier study can only provide us with a rough estimate of the dynein stall force and is more likely to be lower, rather than higher, than the actual value. Still it is useful to make the comparison, as it points out the similarity of the estimates derived from widely disparate systems.

The sustained high force and active moment exhibited by a bull sperm flagellum in an isometric stall has very interesting implications for the underlying mechanism of the flagellar beat. The stall force for the axoneme as a whole is very close to the maximum force that would be contributed if all of the dynein heads were to pull at the same time. This strongly suggests that all of the dyneins in a working segment of axoneme pull simultaneously. An analogy to this would be that the heads are like oxen working in a team; each is fully capable of hauling a share of the load. This contrasts with the view of the dynein arm as a complex motor that somehow functions as a unit. Furthermore, the sustained force output shows that they must continue to pull as long as the stall is maintained. The force-producing step of the cross-bridge cycle must be extended almost indefinitely in the isometric condition of zero shear velocity. Both of these conclusions are of interest in understanding the way in which dynein behaves within the confines of a functional axoneme.

The indefinite extension of the force-producing step of the dynein duty cycle by blocking the beat is compatible with the suggestion of Murase (1990, 1991) that the dynein duty cycle and the flagellar beat cycle are linked. It is also compatible with the prediction of the Geometric Clutch hypothesis that dynein detachment from the binding sites on the B subtubule will not take place if bend formation is interrupted (Holcomb-Wygle et al., 1999). Data on the dynein cross-bridge cycle derived from in vitro studies have been interpreted to suggested a short duty cycle (Johnson, 1985; Hamasaki et al., 1995; Wang et al., 1995). However, other investigators have shown that at least the inner arm dyneins are processive (Shingyoji et al., 1998; Sakakibara et al., 1999). Our data tend to support the second view. The force data presented here suggest that even if the free running duty cycle is short, the duty cycle would have to become very long under maximum load.

We are also left with another puzzle. To reconcile the in vitro and in situ force data, we must first select the highest in vitro measurements as the correct ones (Shingyoji et al., 1998). Moreover, we must insist that all of the dynein heads must contribute force, not just one per dynein arm. This runs counter to the conception that only a small fraction of the heads are active at a given time (Johnson, 1986; Hamasaki et al., 1995). However, if we do not accept this assertion, then we are left with the equally difficult proposition that the intact arms must be much more powerful than can be justified by the in vitro data on isolated dynein. These are surprising but unavoidable conclusions.

We thank Adair Oesterle at Sutter Instrument Company for her generous technical support in the fabrication of the probes, and John Lafeber at Ann Arbor MultiVision for the use of the Matrox Meteor II card and Inspector 3.0 software used to compose Fig. 1.

This work was supported by grant MCB-9722822 from the National Science Foundation.

REFERENCES

Ashkin, A., K. Shultze, J. M. Dziedzic, U. Euteneur, and M. Schliwa. 1990. Force generation of organelle transport measured in vivo by an infrared laser trap. *Nature.* 348:346–348.

Brokaw, C. J. 1972. Computer simulation of flagellar movement. I. Demonstration of stable bend propagation and bend initiation by the sliding filament model. *Biophys. J.* 12:564–586.

Brokaw, C. J. 1999. Computer simulation of flagellar movement. VII. Conventional but functionally different cross-bridge models for inner and outer arm dyneins can explain the effects of outer arm dynein removal. *Cell Motil. Cytoskeleton.* 42:134–148.

Fawcett, D. W., and D. M. Phillips. 1969. The fine structure and development of the neck region of the mammalian spermatozoon. *Anat. Rec.* 165:153–184.

Hamasaki, T., M. E. J. Holwill, K. Barkalow, and P. Satir. 1995. Mechanochemical aspects of axonemal dynein activity studied by in vitro microtubule translocation. *Biophys. J.* 69:2569–2579.

Holcomb-Wygle, D. L., K. A. Schmitz, and C. B. Lindemann. 1999. Flagellar arrest behavior predicted by the geometric clutch model is confirmed experimentally by micromanipulation experiments on reactivated bull sperm. *Cell Motil. Cytoskeleton.* 44:177–189.

Johnson, K. A. 1985. Pathway of the microtubule-dynein ATPase and the structure of dynein: a comparison with actomyosin. *Annu. Rev. Biophys. Biophys. Chem.* 14:161–188.

Johnson, K. A. 1986. Dynein structure and function. *J. Cell Sci. Suppl.* 5:189–196.

Kamimura, S., and K. Takahashi. 1981. Direct measurement of the force of microtubule sliding in flagella. *Nature.* 293:566–568.

Lindemann, C. B. 1996. Functional significance of the outer dense fibers of mammalian sperm examined by computer simulations with the geometric clutch model. *Cell Motil. Cytoskeleton.* 34:258–270.

Lindemann, C. B., and I. R. Gibbons. 1975. Adenosine triphosphate-induced motility and sliding of filaments in mammalian sperm extracted with Triton X-100. *J. Cell Biol.* 65:147–162.

Lindemann, C. B., and K. S. Kanous. 1997. A model for flagellar motility. *Int. Rev. Cytol.* 173:1–72.

Lindemann, C. B., W. G. Rudd, and R. Rikmenspoel. 1973. The stiffness of the flagella of impaled bull sperm. *Biophys. J.* 13:437–448.

Murase, M. 1990. Simulation of ciliary beating by an excitable dynein model: oscillations, quiescence and mechano-sensitivity. *J. Theor. Biol.* 146:209–231.

Murase, M. 1991. Excitable dynein model with multiple active sites for large-amplitude oscillations and bend propagation in flagella. *J. Theor. Biol.* 149:181–202.

Oiwa, K., and K. Takahashi. 1988. The force-velocity relationship for microtubule sliding in demembranated sperm flagella of the sea urchin. *Cell Struct. Funct.* 13:193–205.

Olson, G. E., and R. W. Linck. 1977. Observations of the structural components of flagellar axonemes and central pair microtubules from rat sperm. *J. Ultrastruct. Res.* 61:21–43.

Sakakibara, H., H. Kojima, Y. Sakai, E. Katayama, and K. Oiwa. 1999. Inner-arm dynein c of *Chlamydomonas* flagella is a single-headed processive motor. *Nature.* 400:586–590.

Shingyoji, C., H. Higuchi, M. Yoshimura, E. Katayama, and T. Yanagida. 1998. Dynein arms are oscillating force generators. *Nature.* 393: 711–714.

Van Buren, P., S. S. Work, and D. M. Warshaw. 1994. Enhanced force generation by smooth muscle myosin in vitro. *Proc. Natl. Acad. Sci. USA.* 91:202–205.

Wang, Z., S. Khan, and M. P. Sheetz. 1995. Single cytoplasmic dynein molecule movements: characterization and comparison with kinesin. *Biophys. J.* 69:2011–2023.

Yoneda, M. 1960. Force exerted by a single cilium of *Mytilus edulis*. I. *J. Exp. Biol.* 37:461–468.